# *Multiscale high-speed photoacoustic microscopy based on free-space light transmission and MEMS scanning mirror*

**CHEN ZHANG,[1,†] HUANGXUAN ZHAO,[1,2,†] SONG XU,[3,†] NINGBO CHEN,[1] KE LI,[1,2] XINKUAN JIANG,[1] LIANGJIAN LIU,[1] ZHICHENG LIU,[2] LIDAI WANG,[4] KENNETH K. Y. WONG,[5] JUN ZOU,[3,*] CHENGBO LIU[1,*] LIANG SONG[1,*]**

*[1]Research Laboratory for Biomedical Optics and Molecular Imaging, Shenzhen Key Laboratory for Molecular Imaging, Guangdong Provincial Key Laboratory of Biomedical Optical Imaging Technology, CAS Key Laboratory of Health Informatics, Shenzhen Institutes of Advanced Technology, Chinese Academy of Sciences, Shenzhen, China*
*[2] Capital Medical University, School of Biomedical Engineering, Beijing, China*
*[3]Texas A&M University, Department of Electrical and Computer Engineering, College Station, Texas, United States*
*[4]City University of Hong Kong, Department of Mechanical and Biomedical Engineering, Hong Kong, China*
*[5]The University of Hong Kong, Department of Electrical and Electronic Engineering, Hong Kong, China*
**Corresponding author: junzou@tamu.edu, cb.liu@siat.ac.cn, liang.song@siat.ac.cn*
*†Authors contributed equally to this work*

**Conventional photoacoustic microscopy (PAM) system makes tradeoffs between lateral resolution and imaging depth, limiting its applications in biological imaging *in vivo*. Here, we present an integrated optical-resolution (OR) and acoustic-resolution (AR) multiscale PAM based on free-space light transmission and fast MEMS scanning. The lateral resolution for OR is 4.9 μm, and AR is 114.5 μm. The maximum imaging depth for OR is 0.7 mm, and AR is 4.1 mm. The imaging speed can reach 50k Alines per second. The high SNRs and wavelength throughput are achieved by delivering light via free-space, and the high-speed is achieved by a MEMS scanning mirror. The blood vasculature from superficial skin to the deep tissue of a mouse leg was imaged *in vivo* using two different resolutions to demonstrate the multiscale imaging capability.**

Photoacoustic microscopy (PAM) is an emerging imaging technique that combines strong optical absorption contrast and high ultrasound penetration. It has been applied successfully to image *in vivo* biological structures and functions that scale from organelles to organs [1]. Based on different lateral resolutions, PAM is divided into optical-resolution (OR) PAM and acoustic-resolution (AR) PAM. The OR-PAM achieves optical-diffraction-limited lateral resolution with a maximum imaging depth of about 1 mm [2]. In contrast, AR-PAM achieves tens of micrometers lateral resolution with a maximum imaging depth of several millimeters [3]. To fully explore the capability of multiscale imaging of PAM, several integrated systems have been presented in the literature [4-7]. In some of these approaches [4-6], a single-mode fiber or a multimode fiber was used for delivering OR light, and a multimode fiber or a fiber bundle was used for delivering AR light. The light transmission efficiency of fiber or fiber bundle is generally limited (e.g., below 50% for single fiber), leading to low laser excitation energy on the sample and low signal-noise ratio (SNR) of the imaging, especially for fast imaging application when using a high-repetition-rate laser with limited pulse energy output. In addition, the image acquisition time in the previous approaches [4-5, 7] was too long to be applied for real-time imaging because of the utilization of mechanical scanning. Fast imaging has been shown to be a key factor for acquiring dynamic and functional information of the tissue under study [8-10]. Hence, an efficient integrated system should not only have high lateral resolution and deep penetration, but also have high-efficiency light transmission and high-speed imaging rates. A simultaneous OR-AR-PAM system using a high-speed MEMS scanner has been reported recently based on fiber coupling laser transmission [6]. The imaging speed of the system has been significantly improved compared to previous integrated systems. In this study, we adopted the MEMS scanning but with a free-space light transmission approach that enables higher laser transmission efficiency, higher laser burning threshold, and larger wavelength throughput. More than 80% of the laser energy was transmitted to the distal end of the imaging system for both OR- and AR-PAM modes, which is much higher than conventional approaches using fibers. The high-speed imaging was achieved by fast MEMS scanning. We conducted phantom experiments to validate the performance of this multiscale high-speed system. The blood vasculature images of the mouse leg were acquired to demonstrate the *in vivo* imaging capability of the system.

The schematic of the system is shown in Fig. 1. The light source is a pulsed laser with high-repetition-rate and high-power (Pilot-30,

ZY Laser Science and Technology, Anshan, China). The pulse duration is 8 ns, and the pulse repetition rate of the laser source can be adjusted from 10 to 100 kHz. The laser source has two output ends at 532 and 1064 nm wavelengths, which are used in OR- and AR-PAM mode, respectively. The output beams from the two ends are both reshaped by irises with a diameter of 1 mm. The 532 nm beam is focused by a plano-convex lens (L1), and then spatially filtered by a 50 μm diameter pinhole (PH) placed immediately after the focus point. The diverging laser beam from the pinhole is transformed into a collimated beam using another plano-convex lens (L2), which then reflects onto a dichroic mirror (DM) by a mirror (M1). The 1064 nm beam is defocused and expanded by two plano-convex lenses (L3 and L4) and then transmitted to DM. The two beams are combined at DM which reflects 532 nm and transmits 1064 nm. The combined beam is further deflected by another mirror (M2) and pass through a doublet lens (L5, NA=0.1) and then reflected off the aluminum-coated hypotenuse of a prism (P) and the MEMS scanning mirror before getting irradiated onto the sample (mouse in Fig. 1).

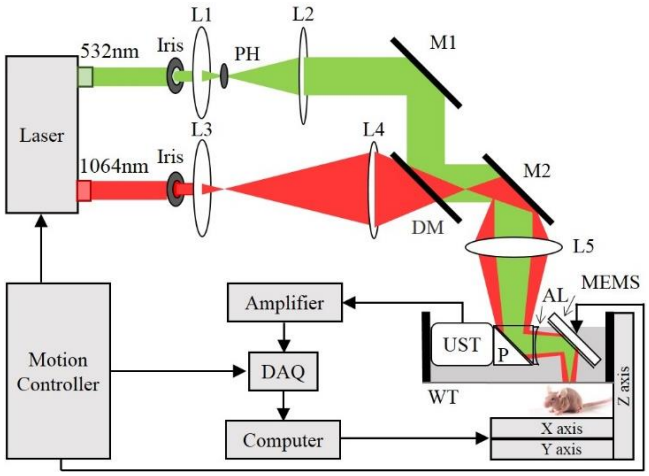


Fig. 1. (Color online) Schematic of the multiscale high-speed PAM system. PH, pinhole; L1, L2, L3, L4, plano-convex lens; L5, doublet lens; M1 and M2, mirrors; DM, dichroic mirror; P, prism; AL, acoustic lens; DAQ, data acquisition card; UST, ultrasound transducer; WT, water tank.

Due to the different optical focusing, the 532 nm beam has a much tighter optical focus than 1064 nm beam on the sample surface. The focus of the acoustic lens (AL, NA=0.28) is in confocal arrangement with the 532 nm beam. The size of the 532 nm focused beam is smaller than that of acoustic focus on the sample surface and hence is termed as OR-PAM. The size of the 1064 nm beam has an optical focus larger than acoustic focus on the sample surface and hence is termed as AR-PAM. The generated photoacoustic signal is received by an ultrasound transducer (UST, V214-BB-RM, Olympus NDT, Central frequency 50MHz, Bandwidth 80%) after reflecting by the MEMS scanning mirror and transmitting through the acoustic lens and two coupled prisms. The prism, the acoustic lens, the MEMS scanning mirror, and the ultrasound transducer are all water-immersed for acoustic coupling to enable the reception of the photoacoustic signals. The received photoacoustic signal is amplified, digitized, and converted into photoacoustic images via Hilbert transformation on a computer. The computer also synchronizes the motion controller of MEMS scanning mirror, motorized stage, data acquisition card (DAQ, CSE1422, GaGe), and laser. The MEMS scanning mirror is house-made which has a mirror plate supported by two hinges made of high-strength flexible polymer materials and actuated by high efficient electromagnetic force [11]. The MEMS worked at a continuous scan in resonance, and the speed and range of the scanning can be adjusted by controlling the frequency and amplitude of the continuous sinusoidal driving voltage. The scanning frequency of the MEMS was set to 50 Hz for all the measurements in this study. The scanning range for the MEMS scanning mirror is 1 mm, and the motorized stage (XY axis) is used to move the sample for scanning range more than 1 mm. The Z-axis of the stage is used for adjusting the imaging plane during the imaging process. To demonstrate the fast imaging speed of MEMS scanning, two crossed tungsten wires each with a diameter of 60 μm were imaged in OR-PAM mode using 532 nm wavelength of laser and the real-time imaging was shown in Visualization 1.

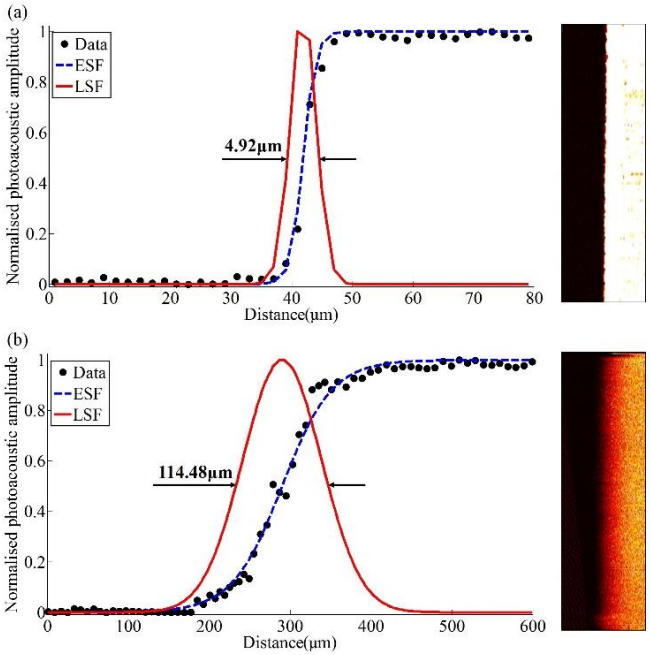


Fig. 2. (Color online) System performance test of the multiscale PAM system. (a) Lateral LSF of the OR-PAM. (b) Lateral LSF of the AR-PAM.

For the resolution measurement, the repetition rate of laser was set at 50 kHz, which corresponds to 50 kHz Aline scanning speed and 2 μm scanning step. The lateral resolutions of OR- and AR-PAM modes were measured by scanning the sharp edge of a blade. The theoretical lateral resolution of OR-PAM and AR-PAM were calculated to be 2.71 μm and 78.72 μm, respectively. The maximum amplitude projection (MAP) images of the blade are shown on the right side in Fig. 2(a) and (b) for OR-PAM and AR-PAM, respectively. The line spread function (LSF) is the first derivative of the edge spread function (ESF) of the corresponding MAP data. The full width at half maximum (FWHM) of the LSF was measured as the lateral resolution. As shown in Fig. 2, the lateral resolution of OR-PAM is 4.92 μm, and AR-PAM is 114.48 μm, respectively. The degrading of the experimentally measured lateral resolutions compared to the theoretical values is presumably due to the

aberration of the optical elements and the defocusing at oblique angles when scanning with the MEMS scanning mirror.

To evaluate the performance of the system for *in vivo* imaging, we conducted a series of experiments on living mice. The repetition rate of laser was set at 10 kHz to enable higher energy output as the pulse energy is inversely proportional to the pulse repetition rate. The reduced repetition rate would though lead to certain decrease of the lateral resolution of OR-PAM (around 24 μm) due to the reduced sampling during MEMS scanning. The pulse energy for *in vivo* OR-PAM and AR-PAM is 800 nJ and 250 μJ respectively, corresponding to the laser fluence of 18 mJ/cm$^2$ and 69 mJ/cm$^2$ at the surface of the sample, which are below the American National Standards Institute (ANSI) safety limit at the corresponding wavelength of 532 nm and 1064 nm. All animal experimental procedures were approved by the Institutional Animal Care and Use Committee of Shenzhen Institutes of Advanced Technology, Chinese Academy of Sciences. Normal 6 to 8-week-old female Balb/C mice were used for *in vivo* experiments. A mixture of 1% vaporized isoflurane and oxygen was continually flowed over the nose mask of the mouse (flow rate is 1 L/min) to keep them anesthetized during the imaging. The mouse was placed on an experimental stage over an electrical heating pad to maintain the body temperature at 37 °C. The ultrasound gel was placed on the imaging region for impedance matching between the bottom of the water tank and the mouse imaging surface.

For mimicking the tumor angiogenesis condition, a conjugated polymer nanoparticle probe (CP NP) with an absorption peak of 1064 nm [12] and matrigel were mixed in the ratio of 1:1, and 30μL mixture was injected subcutaneously into the mouse hind leg to mimic the tumor mass. A 7.7 × 8 mm$^2$ region of the mouse leg was imaged as shown in Fig. 3(a). The top view MAP imaging results at two different modes are shown in Fig. 3(c) and (e), and the side view MAP images are shown in Fig. 3(d) and (f). For OR-PAM, the tightly-focused light gets strongly attenuated before reaching the optical diffusion limit of 1 mm (Fig. 3(d)). For the AR-PAM, the maximum imaging depth in the leg was much higher (Fig. 3(f)) due to the weakly beam focusing and higher laser pulse energy. The merged top view MAP image of OR- and AR-PAM is shown in Fig. 3(b). The vasculature is shown in red, and the mixture is shown in green. By comparing the original photo (Fig. 3(a)) and the merged image (Fig. 3(b)), it can be seen that the multiscale system vividly reflects the underlying anatomy but with more details and higher contrast.

To further evaluate the capability of AR-PAM for vascular imaging for the purpose of tumor angiogenesis application, 100 μL (0.1mg/mL) CP NP was injected intravenously into a mouse via the tail vein. A 10 × 10 mm$^2$ region of the mouse hind leg (Fig. 4(a)) was imaged by OR-PAM and AR-PAM sequentially. As that in Fig. 3, the maximum imaging depths of OR-PAM and AR-PAM in Fig. 4 are different. For OR-PAM, the imaging depth was optically determined and was about 0.71 mm maximally (Fig. 4(d)). For AR-PAM, where the light was weakly focused, and pulse energy was more than 300 times higher than OR-PAM, the generated photoacoustic signals were at about 4.16 mm depth maximally (Fig. 4(f)). Compared to the OR-PAM mode, the AR-PAM mode shows fewer small blood vessels at shallower depth and more vessels at larger depths with inferior resolution. The merged top view MAP image obtained by OR-PAM (Fig. 4(c)) and AR-PAM (Fig. 4(e)) is shown in Fig. 4(b). In this figure, the small and shallow vessels from OR-PAM are shown in green, the large and deep vessels from AR-PAM are shown in red, and the co-registered blood vessels are shown in yellow.

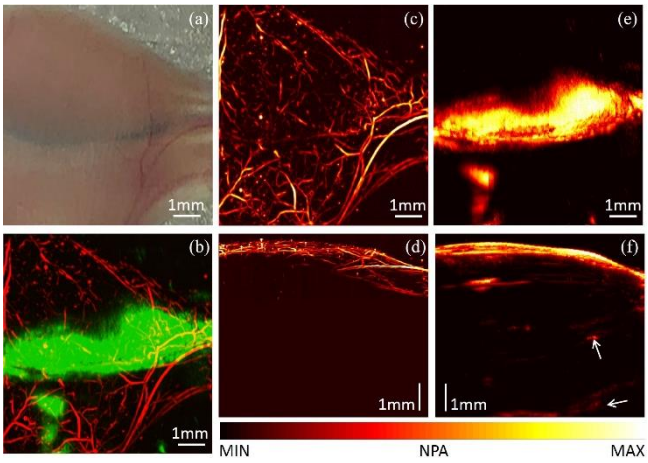


Fig. 3. (Color online) *In vivo* OR and AR images of a mouse hind leg vasculature and a mixture of nanoprobe and matrigel, acquired at 532 nm and 1064 nm wavelength, respectively. (a) Photograph of the mouse leg. (b) Merged image of the top view MAP image with OR-PAM and AR-PAM. (c) and (d) Top and side view MAP images obtained by OR-PAM. (e) and (f) Top and side view MAP images obtained by AR-PAM, and white arrows indicating CP NP signals. NPA, normalized photoacoustic amplitude.

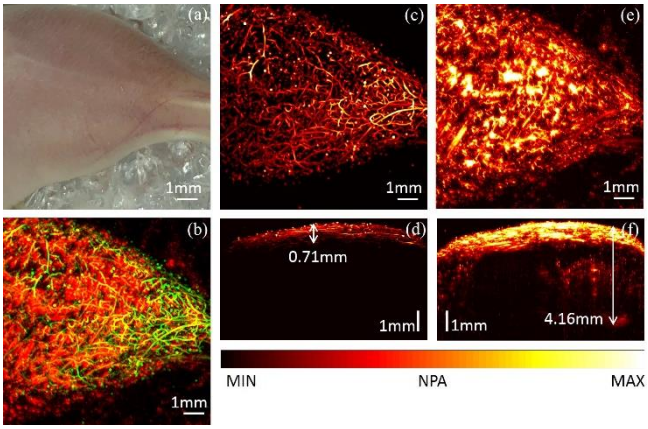


Fig.4. (Color online) *In vivo* OR and AR images of vasculature of a mouse hind leg, acquired at 532 nm and 1064 nm wavelength, respectively. (a) Photograph of the mouse leg. (b) Merged image of the top view MAP image with OA-PAM and AR-PAM. (c) and (d) Top and side view MAP images obtained by OR-PAM. (e) and (f) Top and side view MAP images obtained by AR-PAM.

To the best of our knowledge, this is the first time a high-speed multiscale system combining OR and AR image characteristics has been demonstrated using the MEMS scanning mirror and the light delivered through free-space. The system achieves large imaging depths with high SNR and wavelength throughput by free-space light delivering. The lateral resolution can be switched between 4.9 and 114.5 μm, and the maximum imaging depth can be switched between 0.7 and 4.1 mm. The performance of the system is demonstrated by imaging the phantom as well as the mouse leg *in vivo*. A region of 1 × 1 mm$^2$ with a step size of 10 μm is scanned within 1 s using the MEMS scanning mirror for B-scan and the motorized stage for the other perpendicular direction scanning. A larger field of view can be obtained by stitching multiple datasets

together, e.g., in the above experiment, a FOV of 10 × 10 $mm^2$ was obtained in 14 min. The much longer time is due to slow scanning speed of motorized stage, data storage into DAQ card, and calculation time in data post-processing. Replacement with higher performance motorized stage and DAQ card, or replacing current MEMS with a larger scanning range or 2 axis scanning capability, will enhance the imaging speed of large areas [9-10].

Compared to the OR-AR-PAM system based on fiber transmission, the proposed system has the following key advantages. (1) The free-space light transmission enables higher transmission efficiency, higher burning threshold, and larger wavelength throughput [13-15]. The higher laser transmission efficiency (for OR-PAM mode in specific) enables more laser energy to be transmitted to the sample, enhancing imaging sensitivity and image quality. The image quality of the mouse leg in this study is significantly improved compared to that of mouse back in a previous study using fiber transmission [6]. Hence, the proposed approach could expand the applications of multiscale imaging. The higher burning threshold is very important for high-speed imaging when hundreds of kilohertz or even megahertz laser pulses are used. In this study, the free-space transmission can deliver laser power higher than 100 mW, while the single-mode fiber or multimode fiber with a small core diameter was prone to be burned at lower power [13-14]. Hence, the fiber transmission design would restrain the energy output of the laser source, especially when it works under a high repetition rate. The larger wavelength throughput is extremely important to multicolor photoacoustic imaging to acquire functional and molecular information. A single-mode optical fiber is not feasible to deliver 532 nm and 1064 nm wavelengths simultaneously in OR-PAM without adjusting the optical path due to the optical dispersion obstacle, and hence cannot acquire both signals concurrently. High-power, dispersion-compensated fibers such as single-mode photonic crystal fiber can partially address the issues in power delivery and wavelength dispersion, but the cost is high. The proposed system is fundamentally free of these issues and has advantages considering its high imaging performance, easy implementation, and low cost. (2) While the fiber-based laser transmission has its own advantages such as more compact design, more flexibility and immunity to environmental interference, the free-space transmission is more robust. The biggest challenge compromising the robustness of the published system is the single-mode fiber coupling, which does not exist in the proposed system. To further enhance the robustness of the system, the optical components used for light delivery can be fixed. As a stable system, it is extremely important for translational study to obtain consistent and high-quality images at all times. The proposed approach should represent the future trend for the development of multiscale photoacoustic microscopy.

In summary, a multiscale high-speed PAM system with OR and AR modes is demonstrated successfully here. The integrated system can potentially become a powerful imaging tool for many *in vivo* preclinical applications, including tumor angiogenesis, drug response, brain functions, biomarkers and gene activities. When integrated with a multi-wavelength pulsed laser source with a high pulse repetition rate (such as supercontinuum or Raman pulsed laser) [16], the capability of the system can be further enhanced to obtain both functional and molecular information. Such a system would greatly benefit tumor boundary imaging and brain function study. The accurate profile of the tumor boundary, as well as the infiltration of the tumor in the surrounding tissue, can be mapped accurately by integrating structural (tumor angiogenesis), functional (oxygen metabolism), and molecular information (tumor biomarkers) obtained with our system. For brain function study, besides hemodynamic information, the neural dynamics can also be imaged using our system with appropriate pre-labeling [17]. Thus the multiscale imaging capability of our system would enable direct visualization of brain-wide neuronal activity of large mammalian animals such as mouse.

**Funding.** National Natural Science Foundation of China (NSFC) grants 91739117 and 81927807; Shenzhen Science and Technology Innovation grant JCYJ20170413153129570; Chinese Academy of Sciences grant YJKYYQ20190078, 2019352 and GJJSTD20180002; China Postdoctoral Science Foundation grant 2018M643260.

**Disclosures.** The authors declare no conflicts of interest.

## References

1. L. V. Wang and S. Hu, Science **335**, 1458 (2012).
2. S. Hu, K. Maslov and L. V. Wang, Opt. Lett. **36**, 1134(2011).
3. A. Jathoul, J. Laufer, O. Ogunlade, B. Treeby, B. Cox, E. Zhang, P. Johnson, A. Pizzey, B. Philip, T. Marafioti, M. Lythgoe, R. Pedley, M. Pule and P. Beard, Nat. Photonics **9**, 239 (2015).
4. W. Xing, L. Wang, K. Maslov and L. V. Wang, Opt. Lett. **38**, 52 (2013).
5. B. Jiang, X. Yang, Y. Liu, Y. Deng and Q. Luo, Opt. Lett. **39**, 3939 (2014).
6. M. Moothanchery, R. Bi, J. Kim, G. Balasundaram, C. Kim and M. Olivoa, J. Biomed. Opt. **24**, 086001 (2019).
7. W. Liu , D. M. Shcherbakova, N. Kurupassery, Y. Li, Q. Zhou, V. V. Verkhusha and J. Yao, Scientific Reports **8**, 11123 (2018).
8. J. Yao, L. Wang, J. Yang, K. Maslov, T. Wong, L. Li, C. Huang, J. Zou and L. V. Wang. Nat. Methods **12**, 407 (2015).
9. B. Lan, W. Liu, Y. Wang, J. Shi, Y. Li, S. Xu, H. Sheng, Q. Zhou, J. Zou, U. Hoffmann, W. Yang and J. Yao, Biomed. Opt. Express **9**, 4689 (2018).
10. J. Kim, C. Lee, K. Park, G. Lim and C. Kim, Scientific Reports, **5**, 7932 (2015).
11. S. Xu, C. Huang and J. Zou, J. Micro/Nanolithography, MEMS, and MOEMS **14**, 035004 (2015).
12. B. Guo, J. Chen, N. Chen, E. Middha, S. Xu, Y. Pan, M. Wu, K. Li, C. Liu and B. Liu, Adv. Mater. **31**, 1808355 (2019).
13. J. Yao and L. V. Wang, Photoacoustics **2**, 87 (2014).
14. M. Moothanchery, R. Bi, J. Kim, S. Jeon, C. Kim and M. Olivo, Biomed. Opt. Express **9**, 1190 (2018).
15. Wang Y, Hu Y, Peng B, H. Zhou, Y. Zhao and Z. Ma, Biomed. Opt. Express **11**, 505 (2020).
16. Y. Liang, L. Jin, B. Guan and L. Wang, Opt. Lett. **42**, 1452 (2017).
17. S. Gottschalk, O. Degtyaruk, B. Larney, J. Rebling, M. Hutter, X. Deán-Ben, S. Shoham, D. Razansky. Nat. Biomed. Eng. **3**, 392 (2019).

## Full references


[1] Wang L V, Hu S. Photoacoustic tomography: *in vivo* imaging from organelles to organs [J]. Science, 2012, 335(6075): 1458-1462.

[2] Hu S, Maslov K, Wang L V. Second-generation optical-resolution photoacoustic microscopy with improved sensitivity and speed [J]. Optics letters, 2011, 36(7): 1134-1136.

[3] Jathoul A P, Laufer J, Ogunlade O, et al. Deep *in vivo* photoacoustic imaging of mammalian tissues using a tyrosinase-based genetic reporter [J]. Nature Photonics, 2015, 9(4): 239.

[4] Xing W, Wang L, Maslov K, et al. Integrated optical-and acoustic-resolution photoacoustic microscopy based on an optical fiber bundle [J]. Optics letters, 2013, 38(1): 52-54.

[5] Jiang B, Yang X, Liu Y, et al. Multiscale photoacoustic microscopy with continuously tunable resolution [J]. Optics letters, 2014, 39(13): 3939-3941.

[6] Moothanchery M, Bi R, Kim J Y, et al. High-speed simultaneous multiscale photoacoustic microscopy[J]. Journal of biomedical optics, 2019, 24(8): 086001.

[7] Liu W, Shcherbakova D M, Kurupassery N, et al. Quad-mode functional and molecular photoacoustic microscopy [J]. Scientific reports, 2018, 8(1): 11123.

[8] Yao J, Wang L, Yang J M, et al. High-speed label-free functional photoacoustic microscopy of mouse brain in action[J]. Nature methods, 2015, 12(5): 407.

[9] Lan B, Liu W, Wang Y, et al. High-speed widefield photoacoustic microscopy of small-animal hemodynamics[J]. Biomedical optics express, 2018, 9(10): 4689-4701.

[10] Kim J Y, Lee C, Park K, et al. Fast optical-resolution photoacoustic microscopy using a 2-axis water-proofing MEMS scanner[J]. Scientific reports, 2015, 5: 7932.

[11] Xu S, Huang C H, Zou J. Microfabricated water-immersible scanning mirror with a small form factor for handheld ultrasound and photoacoustic microscopy[J]. Journal of Micro/Nanolithography, MEMS, and MOEMS, 2015, 14(3): 035004.

[12] Guo B, Chen J, Chen N, et al. High-Resolution 3D NIR-II Photoacoustic Imaging of Cerebral and Tumor Vasculatures Using Conjugated Polymer Nanoparticles as Contrast Agent[J]. Advanced Materials, 2019, 31(25): 1808355.

[13] Yao J, Wang L V. Sensitivity of photoacoustic microscopy[J]. Photoacoustics, 2014, 2(2): 87-101.

[14] Moothanchery M, Bi R, Kim J Y, et al. Optical resolution photoacoustic microscopy based on multimode fibers[J]. Biomedical Optics Express, 2018, 9(3): 1190-1197.

[15] Wang Y, Hu Y, Peng B, et al. Complete-noncontact photoacoustic microscopy by detection of initial pressures using a 3×3 coupler-based fiber-optic interferometer[J]. Biomedical Optics Express, 2020, 11(1): 505-516.

[16] Liang Y, Jin L, Guan B O, et al. 2 MHz multi-wavelength pulsed laser for functional photoacoustic microscopy[J]. Optics letters, 2017, 42(7): 1452-1455.

[17] Gottschalk S, Degtyaruk O, Mc Larney B, et al. Rapid volumetric optoacoustic imaging of neural dynamics across the mouse brain[J]. Nature biomedical engineering, 2019, 3(5): 392.